

Disorder and Defect Healing in Graphene on Ni(111)

Peter Jacobson,^{*,†,‡} Bernhard Stöger,[‡] Andreas Garhofer,[‡] Gareth S. Parkinson,[‡] Michael Schmid,[‡] Roman Caudillo,[§] Florian Mittendorfer,[‡] Josef Redinger,[‡] and Ulrike Diebold[‡]

[†]Department of Physics, Tulane University, New Orleans, Louisiana 70118, United States

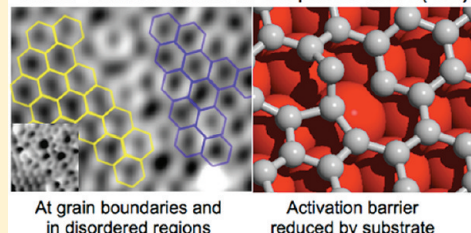
[‡]Institute of Applied Physics, Vienna University of Technology, Vienna, Austria

[§]Intel Corporation, Components Research, 2501 NW 229th Avenue, RA3-252, Hillsboro, Oregon 97124, United States

ABSTRACT: The structural evolution of graphene on Ni(111) is investigated as a function of growth temperature by scanning tunneling microscopy (STM). Low temperature (400–500 °C) growth results in a continuous but highly defective film with small ordered graphene domains and disordered domains composed of Stone–Wales (SW)-like defects. As the growth temperature is increased, the disordered domains shrink leaving small clusters of defects alongside epitaxially matched graphene. Density functional theory (DFT) calculations indicate the crucial role of the metallic support for the healing of SW defects, as the interaction with the substrate leads to a stabilization of the reaction intermediate. This work highlights the effect of the graphene–substrate interaction on the temperature dependence of the defect concentration in epitaxial graphene on Ni(111).

SECTION: Surfaces, Interfaces, Catalysis

Stone-Wales Defects in Graphene on Ni(111)



The prototypical two-dimensional material graphene exhibits a unique suite of electronic properties resulting from its Dirac fermions.^{1,2} These exotic properties were first observed using mechanically exfoliated graphene transferred onto SiO₂, whereas graphene grown by chemical vapor deposition (CVD) on metals then transferred to an insulator exhibits less robust performance.³ Structural defects in graphene may strongly influence the local electronic structure and mechanical properties resulting in conflicting measurements of physical properties.^{2,4,5} Transmission electron microscopy (TEM) and scanning tunneling microscopy (STM) studies of CVD-grown graphene reveal polycrystalline films, resulting from the coexistence of numerous rotational domains.^{6–8} The atomic rearrangement at grain boundaries is typified by the formation of Stone–Wales (SW) defects consisting of pentagon–heptagon pairs. While the structure and properties of grain boundaries is currently of great interest, defects extending beyond the grain boundary have rarely been studied because no reliable production method has been identified. Freestanding graphene has recently been transformed into amorphous graphene by electron bombardment in a TEM,⁹ but such methods are not amenable to widespread study. In this Letter we describe the evolution of defect structures in graphene grown by CVD on Ni(111) as a function of growth temperature. Growth at low temperatures results in an amorphous carbon film with defects similar to the SW variety, while growth at sequentially higher temperatures results in smaller defective areas and domains in registry with the substrate. This process culminates at 650 °C, where a 1 × 1 epitaxial film is formed. Density functional theory (DFT) calculations are used to reveal the relevant mechanisms of defect healing for supported and unsupported graphene sheets.

Figure 1 shows STM images of the graphene layer as a function of growth temperature. At 400 °C (Figure 1a), the film is highly defective, with graphene present in 1 nm² patches. The honeycomb structure and SW-type defect structures are clearly visible (Figure 1a,e). In the more defective regions, the major features are bright protrusions and dark holes 2–3 Å higher or lower than the surrounding region. As the growth temperature is increased to 450 °C (Figure 1b), there is an increase in the area covered by epitaxial graphene. Highly disordered regions are still observed, but the protrusions are now less than 1 Å high. When the growth temperature is increased to 500 °C (Figure 1c) the heavily disordered patches and dark holes largely disappear, but the film still contains a high density of protrusions (<1 Å) in small defective clusters. Figure 1d shows 1 × 1 epitaxial graphene grown at 650 °C. Graphene grown under these conditions exhibits a few defects removing the 1 × 1 epitaxy, but otherwise displays excellent long-range order. To further probe the effect of initial growth conditions, a graphene layer grown at 450 °C was subsequently annealed to 650 °C for 15 min (Figure 1f). This annealed film resembles the films grown at 450 and 500 °C (Figure 1b,c).

At the lowest growth temperature, 400 °C, the graphene honeycomb and defect structures are clearly observed. The dark features in the defective areas correspond to irregular ring structures, which expose the Ni(111) substrate, and are thus potential sites for further hydrocarbon decomposition. Some structures in Figure 1a are similar to SW defects, which consist of neighboring five- and seven-membered rings, but this area

Received: November 14, 2011

Accepted: December 19, 2011

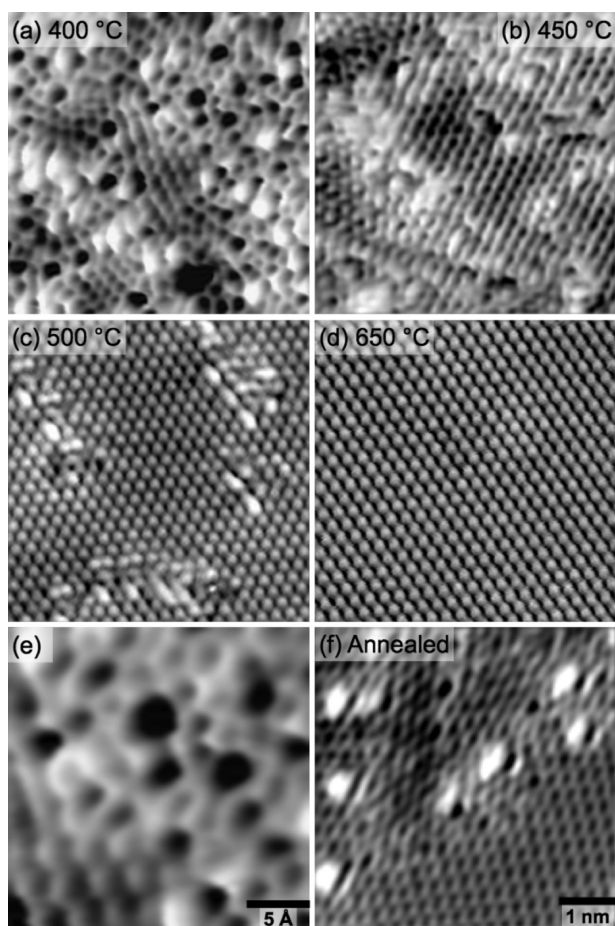


Figure 1. STM images ($6 \times 6 \text{ nm}^2$) of graphene grown at different temperatures: (a) 400 °C, (b) 450 °C, (c) 500 °C (d) 650 °C. (e) Close up ($2.4 \times 2.4 \text{ nm}^2$) of the structure in panel a. (f) Graphene film grown at 450 °C then annealed at 650 °C for 15 min. Tunneling conditions for all images were 5–100 mV, 0.2 nA.

also contains irregular ring structures that are not simply heptagons. Our experiments show that these large, irregular rings are the first structures removed by increasing growth temperature. Annealing the film grown at 450 °C to 650 °C results in epitaxial graphene that is still highly disordered (Figure 1f).

Although we observe SW defects in the structure grown at 400 °C, these defects are not confined to the interface between grains. The coexistence of graphene and disordered areas suggests that amorphous graphene may be the correct designation. The physical properties of amorphous graphene have rarely been investigated experimentally, ostensibly due to lack of production method. Previous theoretical work has investigated planar carbon allotropes, and these calculations predict peculiar electronic structures.¹⁰ Polymorphs such as haeckelite¹¹ and octite SC¹² are predicted to be stable and possess divergent properties: metallic and semiconducting with a 1.2 eV band gap, respectively. Such defective structures may contribute an electronic signature when using nonlocal techniques such as photoemission or transport measurements. Thus, for experiments utilizing CVD-grown graphene on Ni(111), higher growth temperatures should be preferred.

While graphene grown at 650 °C on Ni(111) is largely perfect, we do observe areas with defects such as grain boundaries. Figure 2a shows a polycrystalline region of

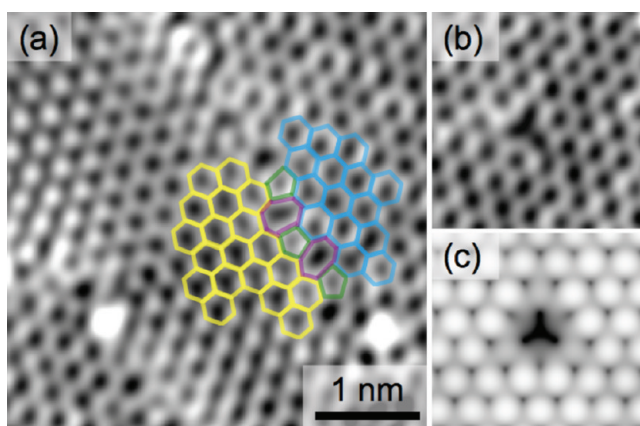


Figure 2. (a) High-resolution image of a graphene grain boundary ($4 \times 4 \text{ nm}^2$). Five- and seven-membered rings observed at the grain boundary and are colored with green and magenta, respectively. (b) An isolated C vacancy on a graphene sheet rotated 21.8° ($2 \times 2 \text{ nm}^2$). (c) Simulated STM image of a single C vacancy in a supported 1×1 graphene sheet.

graphene grown at 650 °C. This area consists of a central graphene region bound by graphene with a moiré pattern resulting from a 21.8° rotation with respect to the Ni(111) surface. Graphene grown at high temperatures results in fewer defects as shown in Figure 1, and while the graphene contains rotational disorder, the lattice is perfect compared to low-temperature growths. When rotationally disordered grains grow together, SW defects may be created at the boundary of the two honeycomb lattices, as seen in Figure 2a. Honeycomb lattices are overlaid on the ordered graphene domains in Figure 2a (yellow and blue overlays) with five- and seven-membered rings at the grain boundary outlined in green and magenta, respectively. The central region consists of graphene without 1×1 epitaxy, the spatially varying appearance in graphene honeycomb results from a small rotation ($<1^\circ$) of the central grain. Figure 2b shows a different region of the graphene grain rotated 21.8° , the moiré structure in this region allows the entire graphene honeycomb lattice to be imaged. At the center of this figure, a single C atom vacancy is imaged, resulting in a dark 3-fold feature. STM simulations indicate that a dark 3-fold depression is present for a C vacancy in 1×1 graphene with a top-face-centered cubic (fcc) binding site (see Figure 2c). While a single C vacancy is the simplest structural defect in graphene, isolated C vacancies were rarely observed on graphene on Ni(111) grown at high temperature (650 °C). A recent study of isolated C vacancies in graphene on Pt(111) required post growth ion bombardment to create C vacancies, indicating that these defects are not prevalent in epitaxially grown graphene.¹³

Our low temperature graphene (400 °C) contains many defects presumably formed during graphene nucleation. To understand the formation and the removal of the defective structures, it is necessary to examine the relevant activation barriers. The properties of the SW defects in the bare graphene layer have been discussed in a recent review,⁴ but little is known about the influence of a supporting substrate.

We have therefore investigated the activation barriers for the removal of an SW defect using DFT calculations. Figure 3 illustrates the reaction pathway for this process. The defect energy of the sinus SW defect (Figure 3a) with respect to the ideal unsupported graphene layer (Figure 3c) is 5.18 eV. This

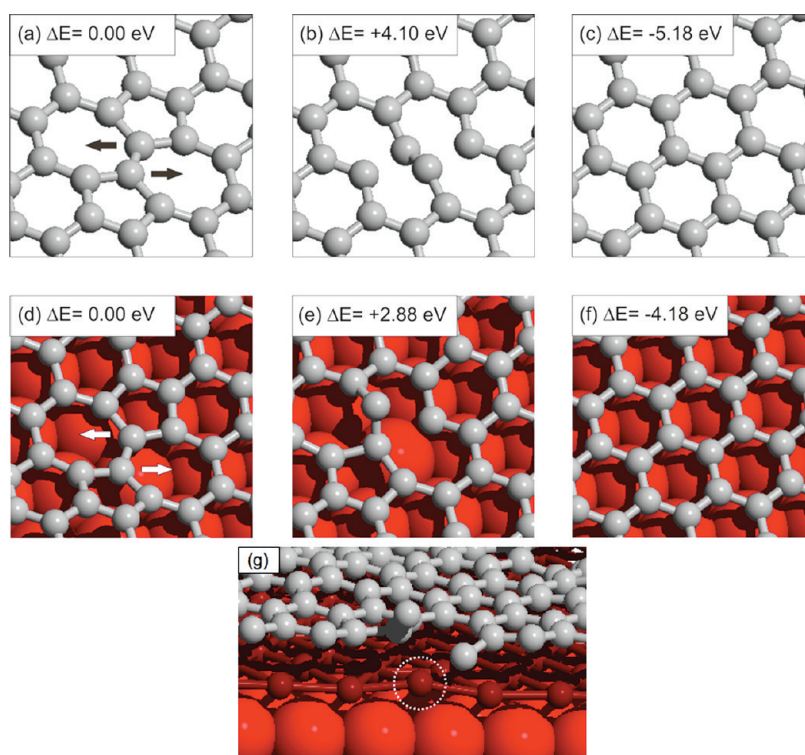


Figure 3. Calculated reaction pathways for the healing of a SW defect for an unsupported graphene sheet (a–c) and graphene on Ni(111) (d–f). Panels b and e display the geometries at the transition state and the 0.37 Å increase in Ni surface corrugation; the affected Ni atom is circled in white. The top Ni layer is shown as a ball and stick model (dark red) to better visualize the corrugation.

value, which is in good agreement with the Perdew–Burke–Ernzerhof (PBE) value of 5.26 eV obtained by Ma et al.,¹⁴ clearly demonstrates a huge thermodynamic driving force for the healing of the layer. However, the process is hindered by a significant barrier of about 4.1 eV, resulting in a kinetic stabilization of the defect. Figure 3(a–c) illustrates the mechanism for the healing of the defects. The high reaction barrier can be understood as the reaction proceeds via a rotation of a C–C pair (Figure 3b), leading to the exposure of two corner atoms of the neighboring graphene rings. It is important to note that the carbon atoms are not rotated *in* the graphene plane, but are rather tilted out of the graphene plane to reduce the compression of the carbon bonds. As a side note, we find that with an energetic cost of 7.7 eV, the formation energy for the second kind of defect, the single C vacancy, is still significantly higher than that for the SW defects.

Although we find a similar mechanism for the healing of the SW defects on the supported graphene sheet, the presence of the Ni substrate significantly alters the energetics of the process. The Ni substrate already leads to a stabilization of the defects in the graphene sheet, as the defect formation energy of 4.18 eV for the SW defect on Ni(111) (Figure 3d) is 1.0 eV lower than for the bare graphene sheet. This energetic stabilization of the defects indicates an enhanced bonding of the defective graphene sheet to the substrate, which can contribute to anchoring this graphene sheet at the surface. Below the supported SW defect, we observe a 0.2 Å corrugation in the Ni atom beneath the on-top C marked in Figure 3d (lower white arrow). Yet, the most striking result is that the reaction barrier is *reduced* from a value of 4.10 to 2.88 eV, even though *less* energy is gained from the reaction. This striking deviation from a traditional Bronsted–Evans–Polanyi relation

is closely related to a modification of the reaction mechanism, this will be discussed in detail below. Even though the barrier of 2.88 eV still implies the need for a temperature of more than 700 °C for a thermal healing of the SW defects on the Ni(111) surface, the barrier of 4 eV for the bare graphene surface would completely suppress this process on the unsupported layer at these temperatures.

Figure 3d–f illustrates how the interaction with the surface also leads to a modification of the reaction mechanism. The key difference is reflected in the geometric structure at the transition state (Figure 3e). While the healing of the SW defect still proceeds via a rotation of a C–C bond, the presence of the surface breaks the symmetry of the process. In contrast to the symmetric out-of-plane tilting of the bond at the transition state in the unsupported graphene layer (Figure 3b), the steric restriction prevents moving the lower C atom closer to the Ni surface. Consequently, while both 5-fold rings are opened simultaneously for the unsupported graphene, one of the 5-fold rings remains closed at the transition state for the Ni supported graphene. The bond between the substrate and the edge of the pentagon is especially pronounced, leading to a C–Ni distance of 1.94 Å and a corrugation of 0.37 Å in the uppermost Ni layer (Figure 3g). Therefore, during the reaction the surface corrugation increases when compared to the supported SW defect. Importantly, we find that all but one undercoordinated edge atom of the reaction intermediate binds to the surface (Figure 3e), leading to a stabilization of the reaction intermediate and thus to an overall reduction of the reaction barrier. It should be also noted that the single vacancies are strongly stabilized by the Ni support. In contrast to the defect energy of 7.7 eV for the unsupported graphene layer, the interaction with the Ni surface reduces the defect

energy to 2.82 eV, making them even more stable than the SW defects. Nevertheless, additional carbon is needed for the removal of the vacancies. This process is closely related to the carbon mass transport, and goes beyond the scope of this paper.

In this study we have demonstrated the structural evolution of graphene on Ni(111) as a function of growth temperature. At low temperatures, the monolayer contains patches of honeycomb graphene, SW-like defects, and large irregular rings. Growth at 650 °C results in highly ordered 1×1 epitaxial graphene. Grain boundaries in graphene grown at high temperature are composed of a combinations of SW defects and strained hexagonal rings. DFT calculations show a new mechanism for the removal of SW defects in supported graphene.

METHODS

STM measurements were performed in an ultrahigh vacuum (UHV) chamber (base pressure 5×10^{-11} mbar) with an Omicron UHV-STM-1 instrument. Prior to CVD growth, the Ni(111) sample was cleaned by repeated sputter/anneal cycles (2 kV Ar⁺, $I_s = 3 \mu\text{A}$, 20 min; 600 °C, 10 min), but, due to C accumulation in the sample after repeated graphene growth, small patches of surface-confined nickel carbide were present on the sputtered and annealed surface. Graphene was grown by the decomposition of toluene ($1\text{--}3 \times 10^{-6}$ mbar, 10 min) at varying temperatures (see Figure 1). The sample temperature was measured via a thermocouple attached to a clip holding the sample plate; the temperature was stabilized at the target temperature before growth. Spin-polarized DFT calculations were performed with the Vienna Ab-initio Simulations Package (VASP),^{15,16} using PAW potentials^{17,18} and the PBE¹⁹ exchange-correlation functional including the van der Waals corrections proposed by Grimme²⁰ with an energy cutoff of 400 eV. The defect energies have been evaluated for a 5×5 surface cell of graphene supported by five layers of Ni using a Ni lattice constant of $r = 3.47 \text{ \AA}$ (i.e., a nearest-neighbor distance of 2.45 Å), where the two uppermost layers were allowed to relax, resulting in residual forces $<0.02 \text{ eV/\AA}$. A $4 \times 4 \times 1$ k-point mesh was employed for the integration of the Brillouin zone. The transition states have been identified with the improved dimer method,²¹ and verified by a subsequent relaxation to the initial (final) state minimum.

AUTHOR INFORMATION

Corresponding Author

*E-mail: jacobson@iap.tuwien.ac.at.

ACKNOWLEDGMENTS

This work was funded by Intel Corporation and the Austrian Science Fund (FWF) within the Wissenschaftskolleg WK04 and the project I422-N16.

REFERENCES

- (1) Geim, A. Graphene: Status and Prospects. *Science* **2009**, *324*, 1530.
- (2) Castro Neto, A. H.; Peres, N. M. R.; Novoselov, K. S.; Geim, A. K. The Electronic Properties of Graphene. *Rev. Mod. Phys.* **2009**, *81*, 109–162.
- (3) Reina, A.; Jia, X.; Ho, J.; Nezich, D.; Son, H.; Bulovic, V.; Dresselhaus, M. S.; Kong, J. Large Area, Few-Layer Graphene Films on Arbitrary Substrates by Chemical Vapor Deposition. *Nano Lett.* **2008**, *9*, 30–35.
- (4) Banhart, F.; Kotakoski, J.; Krasheninnikov, A. V. Structural Defects in Graphene. *ACS Nano* **2011**, *5*, 26–41.
- (5) Grantab, R.; Shenoy, V.; Ruoff, R. Anomalous Strength Characteristics of Tilt Grain Boundaries in Graphene. *Science* **2010**, *330*, 946–948.
- (6) Kim, K.; Lee, Z.; Regan, W.; Kisielowski, C.; Crommie, M.; Zettl, A. Grain Boundary Mapping in Polycrystalline Graphene. *ACS Nano* **2011**, *5*, 2142–2146.
- (7) Huang, P. Y.; Ruiz-Vargas, C. S.; Van Der Zande, A. M.; Whitney, W. S.; Levendorf, M. P.; Kevek, J. W.; Garg, S.; Alden, J. S.; Hustedt, C. J.; Zhu, Y.; et al. Grains and Grain Boundaries in Single-Layer Graphene Atomic Patchwork Quilts. *Nature* **2011**, *469*, 389–392.
- (8) Gao, L.; Guest, J. R.; Guisinger, N. P. Epitaxial Graphene on Cu(111). *Nano Lett.* **2010**, *10*, 3512–3516.
- (9) Kotakoski, J.; Krasheninnikov, A.; Kaiser, U.; Meyer, J. From Point Defects in Graphene to Two-Dimensional Amorphous Carbon. *Phys. Rev. Lett.* **2011**, *106*, 105505.
- (10) Crespi, V. H.; Benedict, L. X.; Cohen, M. L.; Louie, S. G. Prediction of a Pure-Carbon Planar Covalent Metal. *Phys. Rev. B* **1996**, *53*, 13303–13305.
- (11) Terrones, H.; Terrones, M.; Hernández, E.; Grobert, N.; Charlier, J.; Ajayan, P. New Metallic Allotropes of Planar and Tubular Carbon. *Phys. Rev. Lett.* **2000**, *84*, 1716–1719.
- (12) Appelhans, D.; Lin, Z.; Lusk, M. Two-Dimensional Carbon Semiconductor: Density Functional Theory Calculations. *Phys. Rev. B* **2010**, *82*, 073410.
- (13) Ugeda, M.; Fernández-Torre, D.; Brihuega, I.; Pou, P.; Martínez-Galera, A.; Pérez, R.; Gómez-Rodríguez, J. Point Defects on Graphene on Metals. *Phys. Rev. Lett.* **2011**, *107*, 116803.
- (14) Ma, J.; Alfè, D.; Michaelides, A.; Wang, E. Stone–Wales Defects in Graphene and Other Planar sp^2 -Bonded Materials. *Phys. Rev. B* **2009**, *80*, 033407.
- (15) Kresse, G.; Furthmüller, J. Efficiency of Ab-Initio Total Energy Calculations for Metals and Semiconductors Using a Plane-Wave Basis Set. *Comput. Mater. Sci.* **1996**, *6*, 15–50.
- (16) Kresse, G.; Hafner, J. Ab Initio Molecular Dynamics for Liquid Metals. *Phys. Rev. B* **1993**, *47*, 558.
- (17) Blöchl, P. E. Projector Augmented-Wave Method. *Phys. Rev. B* **1994**, *50*, 17953.
- (18) Kresse, G.; Joubert, D. From Ultrasoft Pseudopotentials to the Projector Augmented-Wave Method. *Phys. Rev. B* **1999**, *59*, 1758.
- (19) Perdew, J.; Burke, K.; Ernzerhof, M. Generalized Gradient Approximation Made Simple. *Phys. Rev. Lett.* **1996**, *77*, 3865–3868.
- (20) Grimme, S. Semiempirical GGA-Type Density Functional Constructed with a Long-Range Dispersion Correction. *J. Comput. Chem.* **2006**, *27*, 1787–1799.
- (21) Heyden, A.; Bell, A. T.; Keil, F. J. Efficient Methods for Finding Transition States in Chemical Reactions: Comparison of Improved Dimer Method and Partitioned Rational Function Optimization Method. *J. Chem. Phys.* **2005**, *123*, 224101.